Asian Journal of Chemistry; Vol. 37, No. 7 (2025), 1697-1706

ASIAN JOURNAL OF CHEMISTRY

https://doi.org/10.14233/ajchem.2025.33928

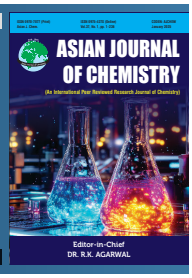

Photocatalytic and Antimicrobial Activities of WO_3, $NdWO_3$ and rGO/$NdWO_3$ Nanoparticles for Environmental and Health Applications

SIVARAJAKRISHNAN ANANDABASKARAN, VIJAYAKUMAR UTHIRAVEL and KRISHNASAMY KUPPUSAMY*

Department of Chemistry, Annamalai University, Annamalai Nagar, Chidambaram-608002, India

*Corresponding author: E-mail: srkalpha777@gmail.com; krishnasamy5699@gmail.com

Received: 27 April 2025; *Accepted*: 12 June 2025; *Published online*: 30 June 2025; AJC-22045

This study explores the synthesis of tungsten trioxide (WO_3), neodymium-doped WO_3 ($NdWO_3$) and reduced graphene oxide/$NdWO_3$ (rGO/$NdWO_3$) composites using a hydrothermal method for efficient photocatalytic degradation of methylene blue dye under natural sunlight. Characterization through XRD, FE-SEM, EDAX, FT-IR, UV-DRS, HR-TEM and XPS techniques confirmed the successful synthesis and structural integrity of the materials. XRD revealed distinct monoclinic and hexagonal structures for WO_3 and $NdWO_3$, while the rGO/$NdWO_3$ composite maintained the crystallinity of both phases. UV-DRS analysis demonstrated a reduction in the band gap from 1.81 eV (WO_3) to 1.60 eV (rGO/$NdWO_3$), enhancing photocatalytic efficiency. Photocatalytic degradation tests indicated rGO/$NdWO_3$ achieved (89.2%) MB removal, outperforming WO_3 (59.4%) and $NdWO_3$ (71.5%). This performance enhancement is attributed to the synergistic interaction between rGO and $NdWO_3$, promoting superior charge separation and electron transfer. The degradation followed pseudo-first-order kinetics with the highest rate constant for rGO/$NdWO_3$ (2.05×10^{-4} min^{-1}). Moreover, antimicrobial assays demonstrated that rGO/$NdWO_3$ exhibited enhanced antibacterial activity against *Staphylococcus aureus*, *Salmonella typhi*, *Escherichia coli* and *Vibrio parahaemolyticus*, surpassing traditional antibiotics. These findings underscore the potential of rGO/$NdWO_3$ as a multifunctional material for advanced photocatalytic and antimicrobial applications.

Keywords: rGO/$NdWO_3$, Hydrothermal method, Methylene blue, Photocatalytic activity, Antimicrobial activity.

INTRODUCTION

The development of efficient photocatalysts for environmental applications, such as wastewater treatment and pollutant degradation, has garnered significant attention in recent years [1-4]. Among various materials, tungsten oxide (WO_3) [5] has emerged as a promising photocatalyst due to its unique properties, including high stability and suitable band gap for photocatalytic reactions. However, its relatively poor charge carrier separation efficiency and limited light absorption, particularly in the visible spectrum, have hindered its performance [6]. To address these limitations, doping WO_3 with neodymium and coupling it with carbon-based materials like reduced graphene oxide (rGO) has proven to enhance its photocatalytic efficiency [7]. Neodymium doping is known to modify the electronic structure and improve charge separation in WO_3, making it a more effective photocatalyst [8]. The incorporation of rGO into WO_3 further contributes to its performance by offering a conductive network, which facilitates the transfer of charge carriers and prevents their recombination.

Metal oxide-based nanoparticles have demonstrated significant antimicrobial activity due to their ability to produce reactive oxygen species (ROS), which are highly detrimental to microbial cells [9]. In particular, vanadium pentoxide (V_2O_5), silver oxide (AgO), yttrium oxide (Y_2O_3) and ytterbium oxide (Yb_2O_3) nanoparticles have been extensively studied for their antimicrobial properties. Reduced graphene oxide (rGO), a two-dimensional material with high surface area and excellent electrical conductivity, has been incorporated into several nanocomposites to enhance the properties of metal oxide nanoparticles. The combination of rGO with metal oxides, such as rGO-V_2O_5, rGO-AgO, rGO-Y_2O_3 and rGO-Yb_2O_3, offers synergistic effects, potentially improving the antimicrobial efficiency of these materials [10].

Ampicillin, a broad-spectrum β-lactam antibiotic, has been a widely used drug for treating bacterial infections. However,

its effectiveness is often compromised due to the emergence of resistant strains of bacteria. As a result, the incorporation of nanoparticles alongside ampicillin could serve as an effective strategy to overcome bacterial resistance. The interaction between nanoparticles and antibiotics can have a synergistic effect, enhancing the antimicrobial action against both Gram-positive and Gram-negative bacteria [11]. Disk diffusion method is a widely used technique for evaluating the antimicrobial activity of various substances, including nanoparticles and antibiotics, like vanadium pentoxide (V_2O_5), rGO-V_2O_5, silver oxide AgO, rGO-AgO, yttrium oxide(Y_2O_3), rGO-Y_2O_3, ytterbium oxide (Yb_2O_3) and rGO-Yb_2O_3 nanoparticles, both individually and in combination with standard antibiotic of ampicillin, using the disk diffusion method [12].

The synergistic effects of Nd-doping and rGO incorporation are expected to enhance the photocatalytic activity of WO_3 [13], particularly in the degradation of organic pollutants under visible light [14,15]. Furthermore, the photocatalytic degradation of methylene blue dye under sunlight is used to assess the performance of these materials. Furthermore, the anti-bacterial properties of the synthesized materials against both Gram-positive and Gram-negative bacterial strains are also evaluated. The findings presented in this paper highlight the potential of rGO/$NdWO_3$ as highly efficient photocatalysts for environmental applications, offering a promising solution for the degradation of organic dyes and other pollutants under sunlight. Comprehensive understanding of the role of Nd-doping and rGO in optimizing the photocatalytic performance of WO_3, contributing to the development of advanced materials for sustainable environmental remediation.

This study focuses on the synthesis and analysis of WO_3, $NdWO_3$ and rGO/$NdWO_3$ nanoparticles, exploring their potential as photocatalysts for the degradation of methylene blue dye under natural sunlight and its antibacterial efficiency. A number of characterization techniques, including XRD, FT-IR, UV-DRS, FE-SEM, EDS, HR-TEM and XPS, were used to confirm the structural integrity and successful synthesis of material. The study reveals that the rGO/$NdWO_3$ composite demonstrated the superior photocatalytic efficiency and antibacterial activity, highlighting its potential for applications in environmental remediation and medical fields, such as wastewater treatment and bacterial disinfection.

EXPERIMENTAL

Sodium tungstate, hydrochloric acid, neodymium(III) nitrate hexahydrate, methylene blue, thiourea and ethanol were obtained from Sigma-Aldrich, USA and the other compounds were used as such without any further purification.

Preparation of graphene oxide: Graphene oxide (GO) was synthesized from graphite powder using the modified Hummers' method [16]. Initially, 1.0 g of graphite powder and 0.5 g of $NaNO_3$ were mixed into 23 mL of cooled conc. H_2SO_4. Gradually, 7.0 g of $KMnO_4$ was added with continuous stirring, while keeping the reaction temperature below 10 ºC using an ice bath. After 0.5 h, the ice bath was removed and the mixture was stirred for an additional 0.5 h at 35 ºC. Distilled water (46 mL) was then added slowly, raising the temperature to 100 ºC, where it was maintained for another 15 min. The reaction was terminated by adding 140 mL of distilled water followed by 10 mL of 30% H_2O_2 aqueous solution. The resulting solid was collected through entrifugation and washed multiple times with 5% HCl solution until no sulfate anions could be detected with $BaCl_2$. The final solid GO was dried under a vacuum at 50 ºC.

Preparation of reduced graphene oxide: To obtain reduced graphene oxide (rGO), the black powder of GO was placed in a 200 mL beaker. Then, 20 mL of hydrazine hydrate was added and the mixture was heated on a hot plate at 100 ºC to 150 ºC. After 15 min, 10-15 mL of water was added dropwise to the mixture, which was then heated until dry. The dried powder was washed and centrifuged multiple times with water and acetic acid, with the pH checked each time to ensure it reached neutral and the product was collected as reduced graphene oxide (rGO) [17].

Synthesis of WO_3 nanoparticles: WO_3 nanoparticles were synthesized using the hydrothermal method. Initially, 2.63 g of sodium tungstate was dissolved in 60 mL of distilled water and the solution was stirred for 10 min at room temperature in a 250 mL beaker. Following this, 20 mL of conc. HCl was added dropwise to neutralize the mixture and then 0.5 g of NaOH dissolved in 10 mL of water, then added to the above mixture by dropwise. This addition caused the transparent solution to turn into a yellowish-white precipitate. The mixture was stirred at room temperature for 0.5 h. It was then transferred to a Teflon-lined autoclave and heated to 130 ºC for 4 h. After the reaction, the product was washed several times with ethanol and distilled water to purify the tungsten oxide nanoparticles [18]. The obtained product was dried and then calcined at 400 ºC for 4 h to yield WO_3 nanoparticles.

Synthesis of neodymium-doped WO_3 and rGO/$NdWO_3$ nanoparticles: Nd-doped tungsten trioxide nanoparticles were synthesized using a hydrothermal method. Initially, 4.12 g of sodium tungstate ($Na_2WO_4{\cdot}2H_2O$) was dissolved in 50 mL of deionized water under constant stirring to prepare the tungstate precursor. To adjust the pH to a slightly acidic range, 16 mL HCl was added to the above mixture. Then, 0.10 g of thiourea was dissolved in 10 mL of water to act as a reducing agent for the tungsten species. Separately, 0.65 g of $Nd(NO_3)_3{\cdot}6H_2O$ was dissolved in 10 mL of deionized water to introduce Nd^{3+} ions into the system. The neodymium precursor was added to the tungstate solution and the mixture was transferred to a Teflon-lined autoclave. The autoclave was sealed and heated at 180 ºC for 12 h to promote the hydrothermal reaction. After the reaction, the product was cooled, filtered and washed with deionized water and ethanol to remove impurities [19]. The resulting Nd-doped WO_3 nanoparticles were dried at 60 ºC for 6 h, then calcined at 400 ºC for 2 h in a muffle furnace before characterization.

For the synthesis of rGO/$NdWO_3$, 30 mg of rGO was added to the $NdWO_3$ solution. The above mentioned procedure of $NdWO_3$ was followed for the preparation of rGO/$NdWO_3$.

Photocatalytic activity: The photocatalytic activity of the synthesized nanomaterials, namely WO_3, $NdWO_3$ and rGO/$NdWO_3$, was evaluated against methylene blue dye under sun-

light irradiation. The nanocatalyst (20 mg) was mixed with 100 mL of 0.3×10^{-4} mol/L methylene blue dye solution and stirred well. At regular intervals (5 mL every 10 min), samples of the sunlight-exposed nanocomposite solutions were withdrawn for absorbance measurement using UV-Vis spectroscopy [20]. The dye degradation efficiency was calculated using the following formula:

$$\text{Degradation efficiency } (\%) = \frac{C_o - C_t}{C_o} \times 100 \quad (1)$$

RESULTS AND DISCUSSION

X-ray diffraction (XRD) studies: X-ray diffraction (XRD) was used to investigate the structural and phase properties of Nd-doped WO_3 combined with reduced graphene oxide (rGO). The XRD pattern of the rGO/$NdWO_3$ composite is shown in Fig. 1. The diffraction peaks in the XRD pattern correspond to distinct phases of WO_3, rGO/$NdWO_3$, confirming the successful incorporation of Nd and rGO into the WO_3 matrix. The XRD patterns of pure WO_3 reveals multiple peaks at 2θ = 23.5º, 33.2º, 35.3º, 49.4º and 55.6º, which correspond to the monoclinic structure of WO_3 as indicated by the JCPDS card (83-0950). These peaks are sharp and well-defined, indicating good crystallinity of the WO_3 phase. After doping with Nd (JCPDS No. 89-2922), additional peaks at 2θ = 29.16º, 30.26º, 32.03º, 59.40º and 60.46 º appear, corresponding to the (101), (004), (102), (114) and (202) planes of Nd, confirming the successful incorporation of Nd into the WO_3 lattice. The presence of these peaks suggests that Nd may substitute for W in the WO_3 matrix. In addition, the XRD pattern of rGO shows a broad peak around 2θ = 26.45º, corresponding to the (002) plane, which indicates a reduced crystallinity typical of rGO. This peak is less sharp compared to that of crystalline graphite, confirming the partial reduction of graphene oxide to rGO. The crystallite sizes of Nd-doped WO_3 and rGO/Nd-WO_3 composite nanoparticles were determined using the Debye-Scherrer's equation:

$$D = \frac{0.9\lambda}{\beta \cos\theta} \quad (1)$$

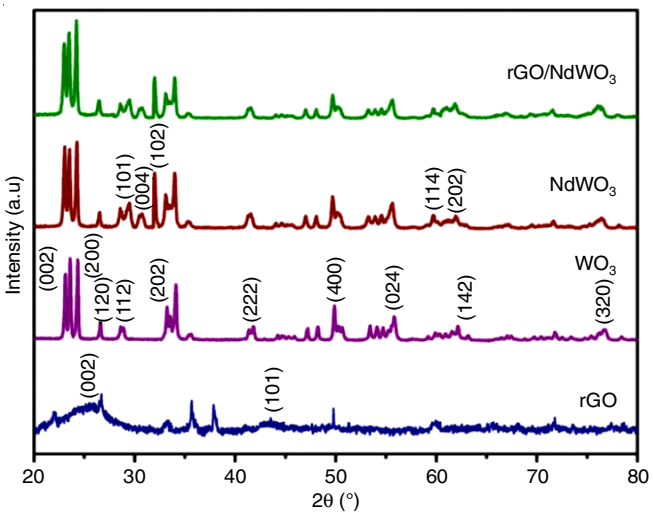

Fig. 1. XRD patterns of (a) rGO, (b) WO_3, (c) $NdWO_3$ and (d) rGO/$NdWO_3$

where λ is the X-ray wavelength; β is the full width at half maximum; θ is the Bragg angle; and D is the average crystallite size. The average crystallite size of WO_3 was calculated to be 12.85 nm, while the crystallite size of Nd-doped WO_3 was determined to be 30.52 nm. The crystallite size of rGO/Nd-doped WO_3 composite was found to be 59.59 nm, indicating that the presence of rGO might facilitate the growth of larger crystallites in the composite structure.

FT-IR studies: FT-IR spectroscopy was used to analyze the bonding characteristics of rGO, WO_3, Nd-doped WO_3 and rGO/$NdWO_3$, as shown in Fig. 2a-d. The FT-IR spectrum of rGO shows a prominent peak at 1631 cm^{-1}, attributed to the C=C stretching vibration [21], along with a band at 2850 cm^{-1}, which corresponds to C–H stretching vibrations, indicating the presence of oxygenated groups on the graphene surface. For WO_3, a strong peak around 650 cm^{-1} is observed, corresponding to the W–O stretching vibration [22], confirming the presence of tungsten oxide. In Nd-doped WO_3, similar W–O stretching vibrations around 767 cm^{-1} are observed. However, slight shift and changes in peak intensities suggest that the incorporation of Nd modifies the WO_3 structure and the local bonding environment. The FT-IR spectrum of rGO/$NdWO_3$ shows the additional peaks from rGO, including the 1631 cm^{-1} band for C=C stretching and the 2850 cm^{-1} band for C–H stretching. These results confirm the successful integration of rGO into Nd-doped WO_3 nanoparticles.

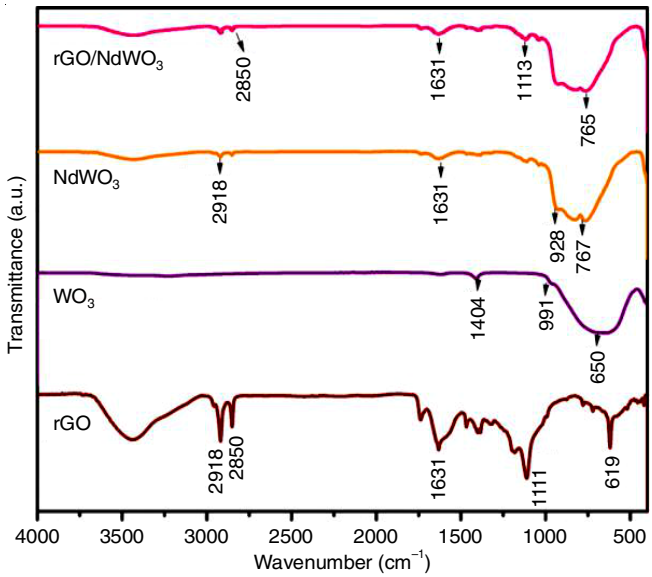

Fig. 2. FT-IR spectra of (a) rGO, (b) WO_3, (c) $NdWO_3$ and (d) rGO/$NdWO_3$

UV-DRS spectra: The UV-DRS spectra for WO_3, Nd-doped WO_3 and rGO/$NdWO_3$ are shown in Fig. 3a-c, respectively. The UV-DRS spectrum of WO_3 reveals strong absorption in the UV region, with a band gap of 1.81 eV, indicative of significant electronic transitions [23]. The spectrum for Nd-doped WO_3 shows a similar absorption behaviour but with a slight redshift, indicating a band gap reduction to approximately 1.75 eV. This decrease in the band gap is attributed to the incorporation of Nd^{3+} ions, which modify the electronic properties of WO_3, enhancing light absorption in the visible spectrum. The

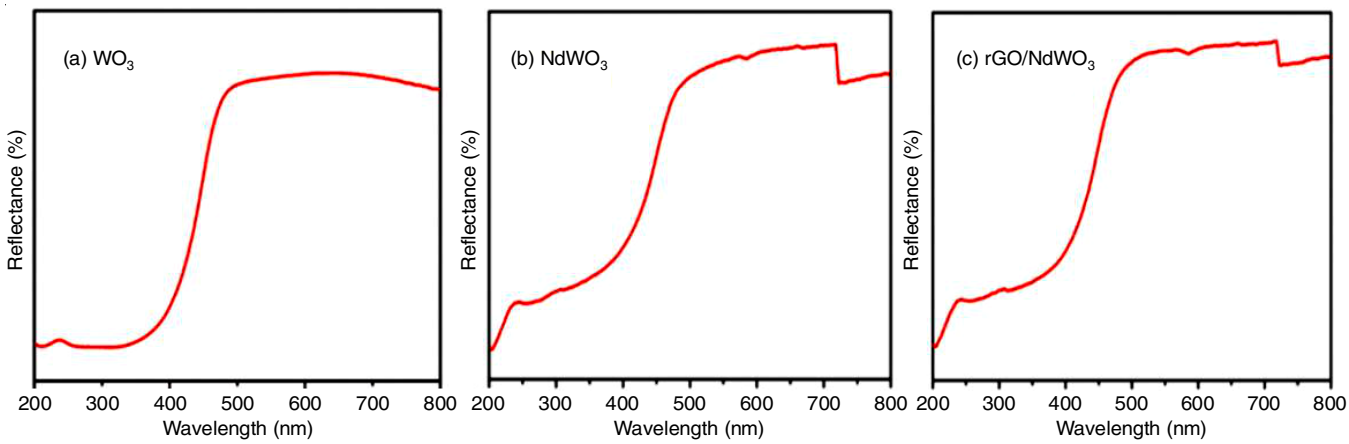

Fig. 3. UV-DRS spectrum of (a) WO_3, (b) $NdWO_3$, (c) rGO/$NdWO_3$

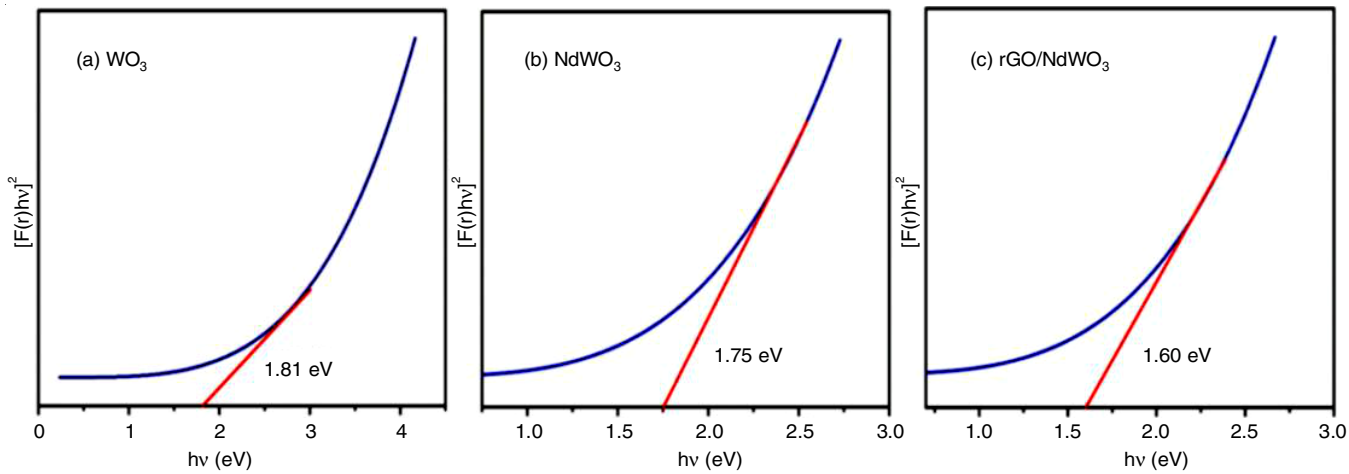

Fig. 4. Tauc plot of (a) WO_3, (b) $NdWO_3$, (c) rGO/$NdWO_3$

UV-DRS spectrum of rGO/$NdWO_3$ demonstrates further enhanced absorption across a broader wavelength range, with an estimated band gap of 1.60 eV. This reduced band gap is primarily due to the synergistic effects of Nd-doping and the presence of reduced graphene oxide (rGO), which improves charge transfer and facilitates photocatalytic activity under visible light. The rGO component further enhances the light absorption capacity, making the composite more efficient for photocatalytic processes.

Tauc plots for WO_3, Nd-doped WO_3 and rGO/$NdWO_3$ were constructed by plotting $(\alpha h\nu)^2$ against photon energy ($h\nu$), as shown in Fig. 4. The extrapolation of the linear regions of these plots to the *x*-axis provides the corresponding band gap values, which align with those obtained from the UV-DRS spectra. The Tauc plots confirm that the band gaps of WO_3, Nd-doped WO_3 and rGO/$NdWO_3$ are 1.81, 1.75 and 1.60 eV, respectively. These results highlight the reduction of the band gap due to Nd doping and the incorporation of rGO, which enhances the photocatalytic performance of the material.

FE-SEM and EDS studies: Figs. 5 and 6 present the FE-SEM and EDS images of the synthesized nanomaterials *viz.*, rGO, WO_3, Nd-doped WO_3 and rGO/$NdWO_3$. The morphology of each material was analyzed using FE-SEM, revealing the distinct structural features. rGO (Fig. 5a) exhibits a sheet-like structure, characteristic of reduced graphene oxide. WO_3 (Fig. 5b) is composed of agglomerated particles, indicative of the typical structure of tungsten oxide. Nd-doped WO_3 (Fig. 5c) displays similar agglomerated particles to pure WO_3 [24], with some variations in size and distribution due to the doping of

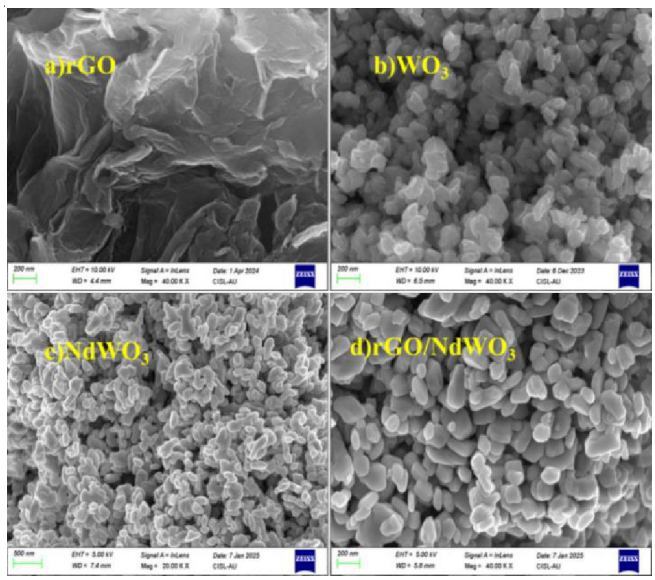

Fig. 5. FESEM surface morphology analysis of (a) rGO, (b) WO_3, (c) $NdWO_3$, (d) rGO/$NdWO_3$

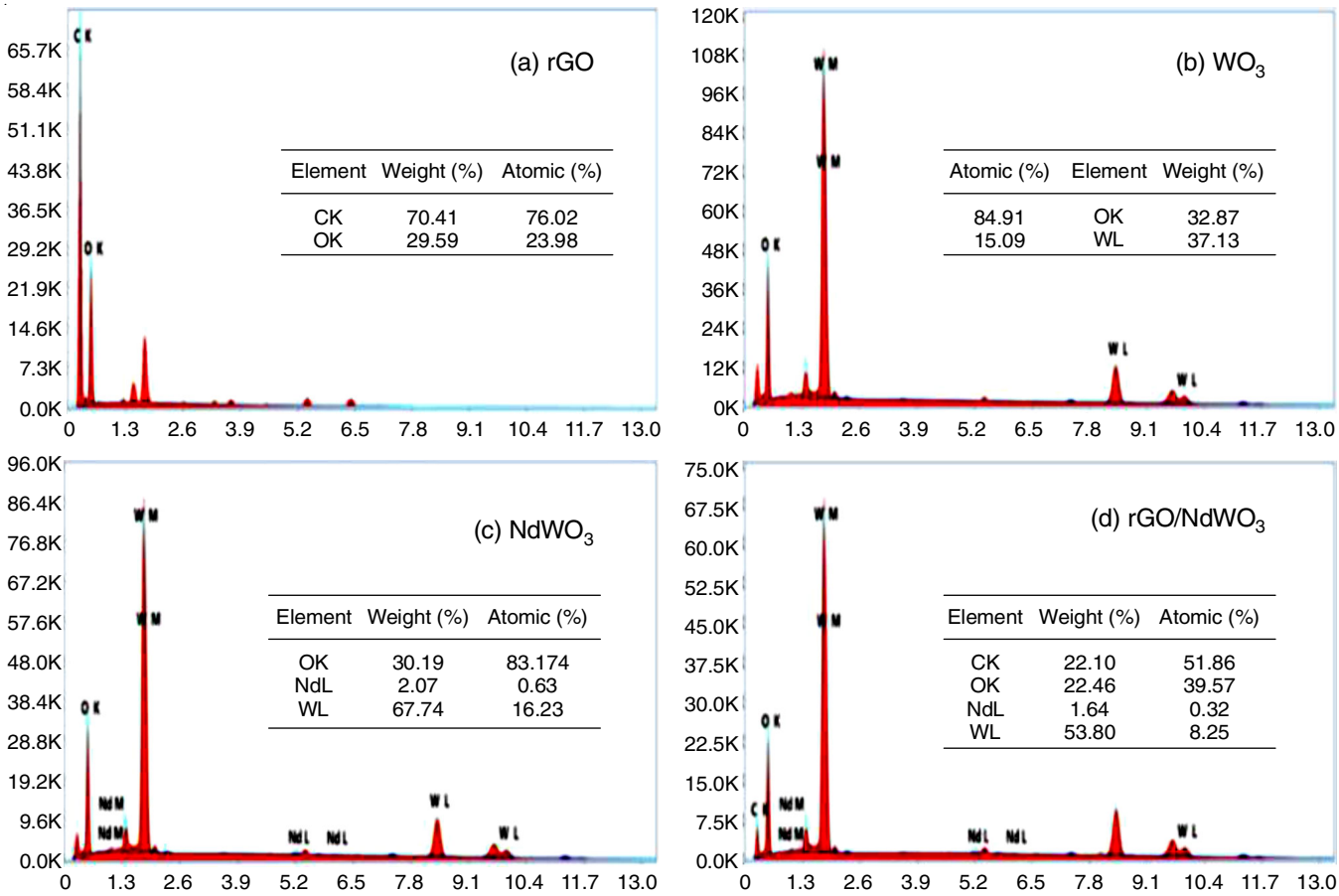

Fig. 6. EDX and Elemental mapping analysis of (a) rGO, (b) WO_3, (c) $NdWO_3$ and (d) rGO/$NdWO_3$

Nd^{3+} ions, which modify the particle arrangement. In contrast, the rGO/$NdWO_3$ composite (Fig. 5d) shows Nd-doped WO_3 particles uniformly distributed over the surface of rGO sheets. This distribution confirms the successful incorporation of Nd-doped WO_3 onto the rGO surface, which is critical for enhancing photocatalytic properties by facilitating charge transfer between the components.

The elemental composition of the synthesized nanomaterials was further analyzed using EDS. The EDS spectra (Fig. 6) confirm the presence of the expected elements in each material. For rGO, peaks corresponding to carbon (C) and oxygen (O) are observed, while WO_3 and Nd-doped WO_3 display peaks for tungsten (W), oxygen (O) and neodymium (Nd) elements are observed. The EDS spectrum for the rGO/$NdWO_3$ composite shows peaks for carbon, tungsten, oxygen and neodymium, validating the successful synthesis and confirming the elemental composition of the rGO/$NdWO_3$ composite.

HR-TEM: The HR-TEM images (Fig. 7a-b) of the rGO/$NdWO_3$ composite reveal distinct structural characteristics. The rGO sheets display a layered structure, with $NdWO_3$ nanoparticles uniformly dispersed across the rGO surface. This unique morphology suggests that rGO effectively supports the $NdWO_3$ particles, preventing aggregation and promoting better interaction between the two components. The dispersion of $NdWO_3$ on rGO likely enhances electronic conductivity and charge separation [24], which could improve the photocatalytic performance of the composite. High-resolution lattice imaging (Fig. 7c) reveals clear lattice fringes corresponding to the $NdWO_3$ phase, with interplanar spacings of approximately 4.31, 1.92 and 1.39 nm, which correspond to the (111), (004) and (204) crystal planes of the $NdWO_3$ structure. This confirms the high crystallinity of the $NdWO_3$ nanoparticles and highlights their well-ordered arrangement within the composite. Although the rGO component is amorphous, it plays a crucial role in supporting the $NdWO_3$ particles and acting as a conductive matrix,

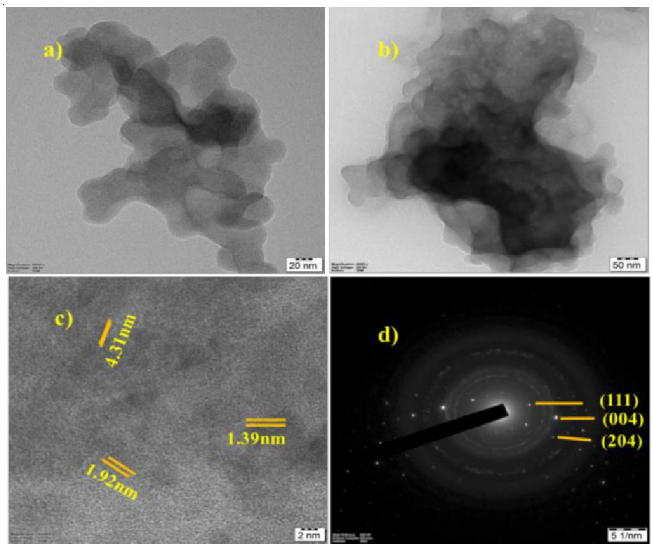

Fig. 7. HR-TEM images, lattice fringes and SAED patterns of rGO/$NdWO_3$

increasing the available active sites for photocatalytic reactions. The selected area electron diffraction patterns (Fig. 7d) further validate the crystalline nature of the rGO/$NdWO_3$ composite, with distinct diffraction spots matching the $NdWO_3$ phase. This confirms the strong crystallographic alignment of $NdWO_3$ within the composite and suggests the material's potential for efficient photocatalytic applications.

XPS: XPS analysis, as shown in Fig. 8 was conducted to determine the elemental composition and the valence states of the elements in the rGO/$NdWO_3$ composite. The survey spectrum for rGO/$NdWO_3$ was collected across the 0 to 1200 eV range, providing valuable information about the surface composition of the material. The W 4*f* spectrum displays two main peaks at binding energies of 35.6 eV and 37.8 eV, which correspond to the W $4f_{7/2}$ and W $4f_{5/2}$ states, respectively. These peaks confirm the presence of tungsten in the +6 oxidation state (W^{6+}) within the WO_3 matrix, indicating that the WO_3 structure remains stable and intact after the incorporation of Nd-doped component. The O 1*s* spectrum exhibits a prominent peak around 530 eV, characteristic of the oxygen in the WO_3 structure. This supports the retention of the WO_3 framework in the composite [25]. A small shoulder at higher binding energies is observed, which may indicate the presence of surface oxygenated groups. These groups likely arise from the interaction between the reduced graphene oxide (rGO) sheets and the Nd-doped WO_3 particles. The C 1*s* spectrum shows a significant peak at 285.68

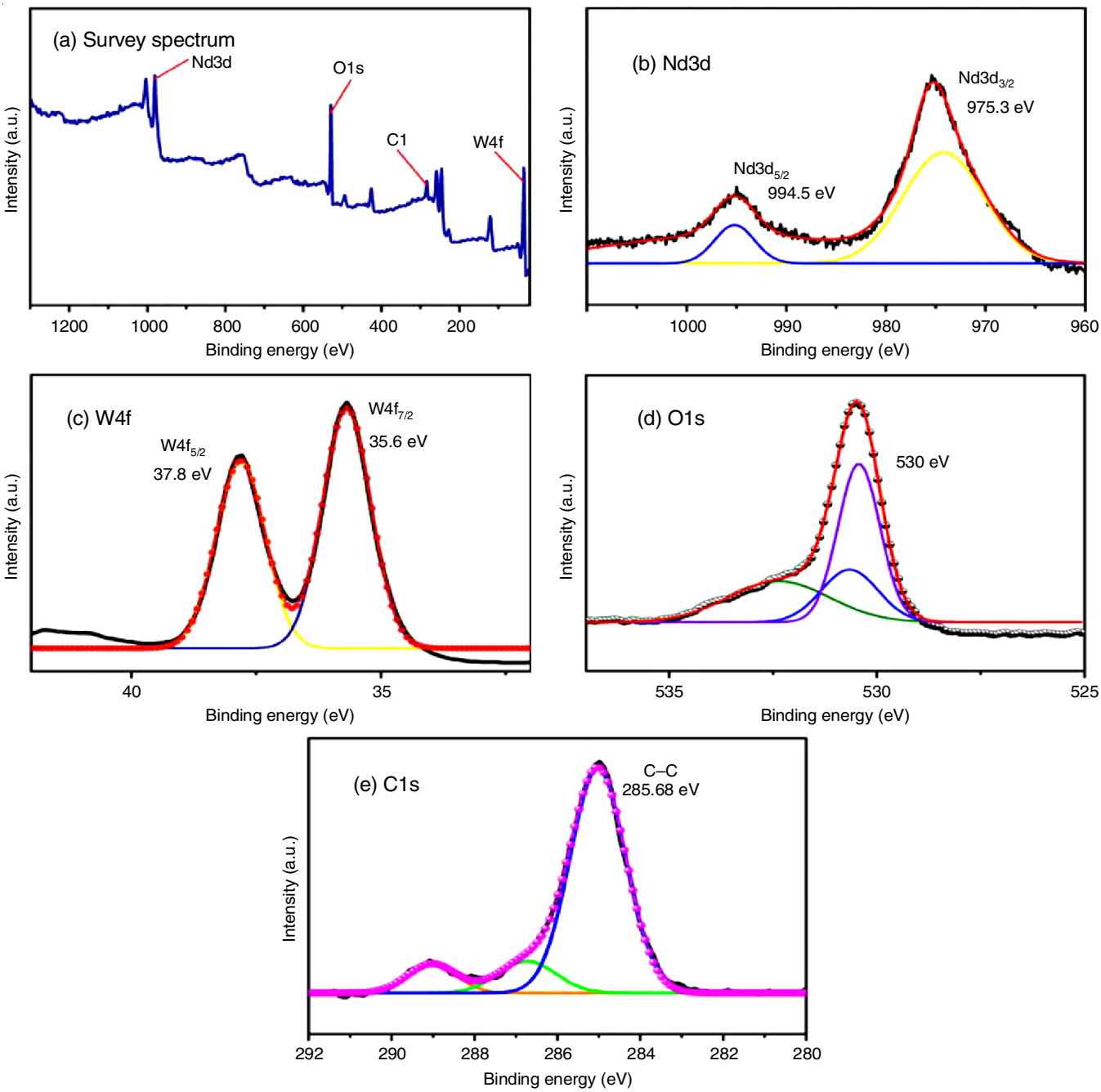

Fig. 8. X-ray photoelectron spectroscopy analysis of rGO/$NdWO_3$

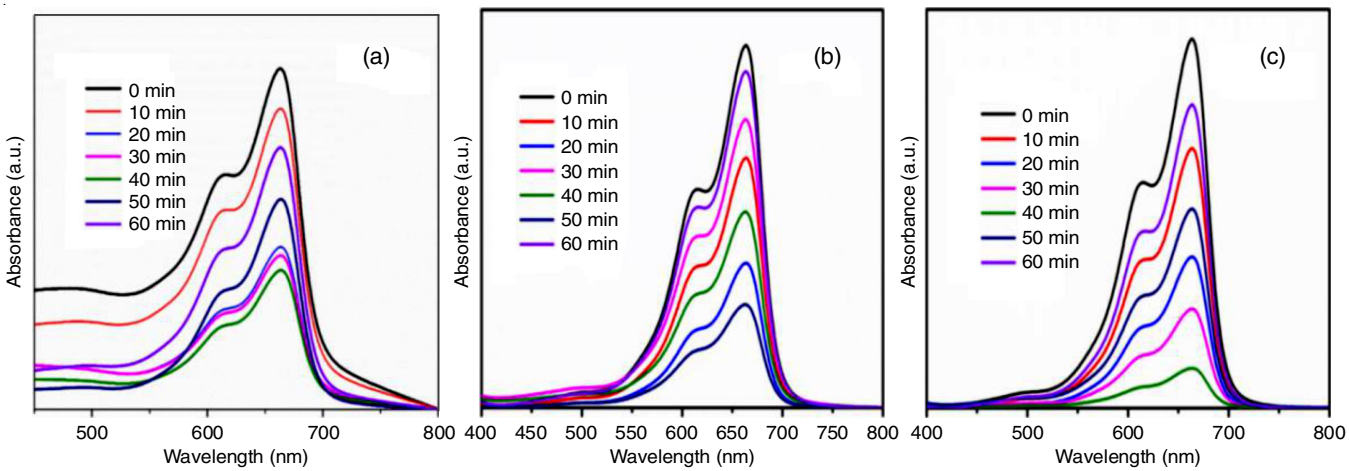

Fig. 9. Photocatalytic degradation of (a) WO_3, (b) Nd-doped WO_3, (c) rGO/$NdWO_3$

eV, attributed to C-C bonds [26], which confirms the successful integration of rGO into the composite [27]. This is consistent with the sheet-like structure of rGO, which interacts with the Nd-doped WO_3 to form the composite material. The Nd 3*d* spectrum confirms the incorporation of neodymium into the WO_3 lattice [28]. Peaks observed at 994.5 and 975.3 eV corresponding to the Nd $3d_{5/2}$ and Nd $3d_{3/2}$ states indicating the successful doping of Nd in its +3 oxidation state (Nd^{3+}). The specific binding energies of these peaks are characteristic of Nd^{3+} in the WO_3 structure, confirming the successful doping process [29]. These XPS results provide critical insights into the elemental composition and oxidation states of the components in the rGO/$NdWO_3$ composite [30].

Photocatalytic activity: The photocatalytic degradation of methylene blue (MB) dye under sunlight has been effectively facilitated using various photocatalysts, including tungsten oxide (WO_3) [31,32], Nd-doped tungsten oxide and reduced graphene oxide (rGO) loaded Nd-doped WO_3 (rGO/$NdWO_3$) composites, as shown in Fig. 9. The photocatalysts performance of WO_3 is 59.4%, Nd-doped WO_3 is 71.5% and rGO/$NdWO_3$ is 89.2% with a catalyst concentration of 20 mg/mL. WO_3 exhibited moderate photocatalytic activity, with a degradation efficiency of 59.4%. This moderate performance can be attributed to its high surface area and good light absorption properties [32,33]; however, WO_3 suffers from limited charge carrier separation efficiency, which hinders its overall photocatalytic performance. Nd-doping of WO_3 resulted in a significant improvement in photocatalytic activity, with Nd-doped WO_3 achieving a degradation efficiency of 71.5%. The incorporation of Nd ions into the WO_3 lattice enhances the charge separation efficiency, broadens the absorption spectrum and introduces additional active sites for photocatalytic reactions [34], leading to better performance compared to undoped WO_3. The addition of reduced graphene oxide to Nd-doped WO_3 (rGO/$NdWO_3$) further enhances the photocatalytic efficiency, achieving a degradation efficiency of 89.2%. The rGO acts as an efficient electron sink, preventing the recombination of charge carriers and thereby facilitating their migration to the surface for redox reactions [35]. Moreover, rGO improves the electronic conductivity and creates additional active sites for the photocatalytic degradation of organic pollutants [36], making rGO/$NdWO_3$ an excellent candidate for methylene blue dye degradation under natural sunlight.

A linear relationship between $\ln(C_o/C_t)$ and time was observed, confirming that the degradation followed pseudo-first-order kinetics (Fig. 10). The rate constants for WO_3, Nd-doped WO_3 and rGO/$NdWO_3$ were calculated to be 1.36, 1.64 and 2.05×10^{-4} min^{-1}, respectively [37]. rGO/$NdWO_3$ exhibited the highest rate constant, demonstrating superior photocatalytic performance. These results suggest that the combination of Nd-doping and rGO incorporation significantly enhances the photocatalytic activity of WO_3, making rGO/$NdWO_3$ highly efficient for dye degradation under sunlight [38]. The photocatalytic degradation mechanism involves the generation of electron-hole pairs when the WO_3, Nd-doped WO_3 and rGO/$NdWO_3$ nanoparticles are exposed to light energy that exceeds their bandgap energy [39]. The excited electrons in the conduction band (CB) can reduce dissolved oxygen to generate superoxide radicals ($O_2^{\bullet-}$), while the holes in the valence band (VB) oxidize water molecules to produce hydroxyl radicals ($^{\bullet}OH$) [40]. These reactive oxygen species (ROS), especially hydroxyl radicals, are

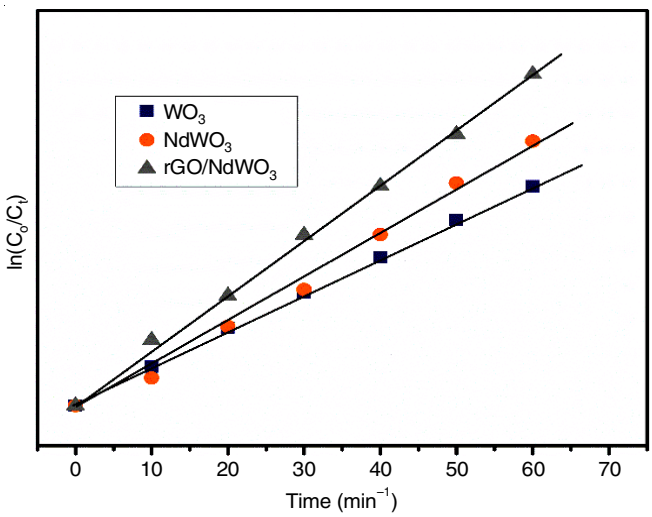

Fig. 10. Pseudo-first order plot of (a) WO_3, (b) Nd-doped WO_3, (c) rGO/$NdWO_3$

powerful oxidizing agents that are responsible for the degradation of organic pollutants, such as methylene blue dye, into non-toxic by products [40]. The primary mechanism for the photodegradation of methylene blue dye is the oxidation by hydroxyl radicals (•OH) and superoxide radicals ($O_2^{\bullet-}$), as shown in the following mechanism (Fig. 11).

In these reactions, hydroxyl radicals (•OH) and superoxide anion radicals ($O_2^{\bullet-}$) play key roles in the oxidation of methylene blue dye, breaking it down into non-toxic byproducts such as CO_2 and H_2O. The rGO/$NdWO_3$ composite benefits from the synergistic effects of Nd-doping and rGO, which significantly enhance its photocatalytic performance under natural sunlight, making it a promising material for environmental cleanup and water purification applications [41].

Antibacterial activity: The antibacterial activity of WO_3, $NdWO_3$ and rGO/$NdWO_3$ nanomaterials was evaluated against a panel of Gram-negative and Gram-positive bacteria at various concentrations (250, 500 and 1000 µg/mL) using the disc diffusion method [42]. The standard antibiotic used was ampicillin. All three nanomaterials exhibited significant inhibitory activity against all tested bacterial strains, for WO_3 as shown in Table-1, WO_3 nanoparticles demonstrated concentration-dependent inhibition against all the tested bacteria [42]. The highest zone of inhibition was observed against *V. parahaemolyticus* (15 mm at 1000 µg/mL), comparable to the zone of inhibition of ampicillin (16 mm) for this bacterium. The $NdWO_3$ nanoparticles also showed concentration-dependent inhibition against all the tested bacteria [43]. The strongest inhibition by $NdWO_3$ was observed against *V. parahaemolyticus* (15 mm at 1000 µg/mL). The strongest inhibition by rGO/$NdWO_3$ was observed against *V. parahaemolyticus* (15 mm at 1000 µg/mL). The enhanced antibacterial activity of rGO/$NdWO_3$ compared to $NdWO_3$ is likely due to synergistic effects. The high surface area of rGO provides a larger surface for nanoparticle deposition, increasing contact with bacteria [44].

Conclusion

In this study, we successfully synthesized and analyzed WO_3, $NdWO_3$ and rGO/$NdWO_3$ nanoparticles, demonstrating their potential as photocatalysts for the degradation of methylene

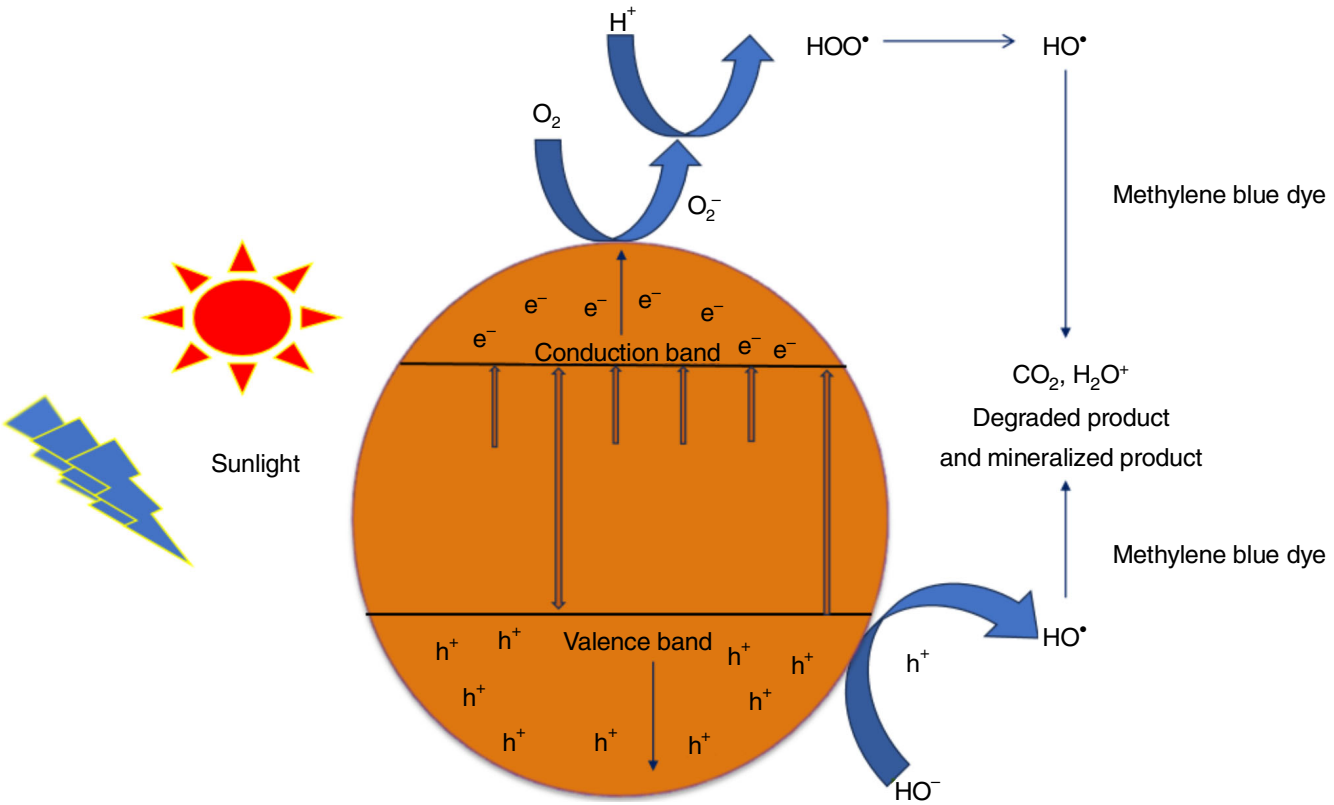

Fig. 11. Schematic illustration of the photo catalytic degradation mechanism

TABLE-1
ANTIBACTERIAL ACTIVITY DATA OF WO_3, $NdWO_3$ AND rGO/$NdWO_3$

Organism	Zone of inhibition (mm) Concentration (µg/mL)									Standard (Ampicillin)		
	WO_3			$NdWO_3$			rGO/$NdWO_3$					
	1000	500	250	1000	500	250	1000	500	250	WO_3	$NdWO_3$	rGO/$NdWO_3$
S. aureus	9	9	8	8	7	6	7	7	4	11	11	11
E. coli	6	6	5	6	6	6	9	6	–	10	10	10
S. typhi	7	6	6	9	8	7	10	7	–	13	13	13
V. parahaemolyticus	15	14	14	15	13	12	15	14	12	16	16	16

blue dye under natural sunlight and as antibacterial agents. Various characterization methods, including XRD, FT-IR, UV-DRS, FE-SEM, EDS, HR-TEM and XPS, were employed to confirm the successful synthesis and structural integrity of the materials. The XRD analysis revealed that WO_3 and $NdWO_3$ exhibited distinct peaks corresponding to their monoclinic and hexagonal structures. The rGO/$NdWO_3$ composite retained the crystalline properties of both phases without significant phase shifts. The crystallite sizes for WO_3, $NdWO_3$ and rGO/$NdWO_3$ were determined to be 12.85, 30.52 and 59.59 nm, respectively. FT-IR spectra confirmed the presence of important functional groups, while UV-DRS analysis showed a decrease in the band gap from 1.81 eV for WO_3 to 1.60 eV for rGO/$NdWO_3$, enhancing the photocatalytic performance under sunlight. FE-SEM and HR-TEM images revealed that $NdWO_3$ was effectively dispersed on the rGO surface, forming a conductive network that enhanced charge transfer. XPS analysis confirmed successful Nd doping in WO_3 and revealed the oxidation states of tungsten and neodymium. Photocatalytic degradation of methylene blue dye was tested and the rGO/$NdWO_3$ composite exhibited the highest degradation efficiency (89.2%) compared to WO_3 and $NdWO_3$ alone. This improvement is attributed to the synergistic effect between rGO and $NdWO_3$, which promoted better charge separation and electron transfer, leading to enhanced photocatalytic activity. The photocatalytic degradation of methylene blue followed pseudo-first-order kinetics, with the highest rate constant observed for rGO/$NdWO_3$ (2.05×10^{-4} min^{-1}). This indicates that the rGO/$NdWO_3$ composite is an effective material for the photocatalytic applications, especially in the degradation of organic pollutants under natural sunlight. These findings emphasize the significance of optimizing composite materials to improve their photocatalytic efficiency, making rGO/$NdWO_3$ a promising candidate for environmental remediation, particularly in wastewater treatment. Furthermore, antimicrobial tests indicated that rGO/$NdWO_3$ exhibited strong antibacterial activity against both Gram-positive and Gram-negative bacterial strains. The rGO/$NdWO_3$ composite holds promise for efficient environmental and medical applications, particularly in water purification and bacterial disinfection.

CONFLICT OF INTEREST

The authors declare that there is no conflict of interests regarding the publication of this article.

REFERENCES

1. C. Byrne, G. Subramanian and S.C. Pillai, *J. Environ. Chem. Eng.*, **6**, 3531 (2018); https://doi.org/10.1016/j.jece.2017.07.080
2. L. Yang, D. Fan, Z. Li, Y. Cheng, X. Yang and T. Zhang, *Adv. Sustain. Syst.*, **6**, 2100477 (2022); https://doi.org/10.1002/adsu.202100477
3. S. Kumari, K. Sharma, S. Korpal, J. Dalal, A. Kumar, Supreet, S. Kumar and S. Duhan, *CrystEngComm.*, **26**, 4886 (2024); https://doi.org/10.1039/D4CE00630E
4. S. Balu, D. Ganapathy, S. Arya, R. Atchudan and A.K. Sundramoorthy, *RSC Adv.*, **14**, 14392 (2024); https://doi.org/10.1039/D4RA01307G
5. J. Akhtar, M.B. Tahir, M. Sagir and H.S. Bamufleh, *Ceram. Int.*, **46**, 11955 (2020); https://doi.org/10.1016/j.ceramint.2020.01.234
6. K. Kalidasan, S. Mallapur, P. Vishwa and S. Kandaiah, *Ind. Eng. Chem. Res.*, **61**, 16673 (2022); https://doi.org/10.1021/acs.iecr.2c02880
7. L. Cui, X. Ding, Y. Wang, H. Shi, L. Huang, Y. Zuo and S. Kang, *Appl. Surf. Sci.*, **391**, 202 (2017); https://doi.org/10.1016/j.apsusc.2016.07.055
8. I. Maryam, T. Iqbal, S. Afsheen and A.M. Ali, *J. Inorg. Organomet. Polym. Mater.*, **33**, 3454 (2023); https://doi.org/10.1007/s10904-023-02776-9
9. U. Kadiyala, N.A. Kotov and J.S. VanEpps, *Curr. Pharm. Des.*, **24**, 896 (2018); https://doi.org/10.2174/1381612824666180219130659
10. T. Subramani and S.K. Nagarajan, *Ceram. Int.*, **50**, 44822 (2024); https://doi.org/10.1016/j.ceramint.2024.08.317
11. M. Arshad, S. Ehtisham-ul-Haque, M. Bilal, N. Ahmad, A. Ahmad, M. Abbas, J. Nisar, M.I. Khan, A. Nazir, A. Ghaffar and M. Iqbal, *Mater. Res. Express*, **7**, 015407 (2020); https://doi.org/10.1088/2053-1591/ab6380
12. S. Kokilavani, S.A. Al-Farraj, A.M. Thomas, H.A. El-Serehy, L.L. Raju and S.S. Khan, *Ceram. Int.*, **47**, 12997 (2021); https://doi.org/10.1016/j.ceramint.2021.01.163
13. A.K. López-Matus, V.W. Velázquez-Vázquez, K.M. Aguilar-Casto, E.V. Macias-Melo, G. Morales-Mendoza, J.Y. Verde-Gómez and R. López-González, *J. Mater. Sci.: Mater. Eng.*, **20**, 75 (2025); https://doi.org/10.1186/s40712-025-00290-z
14. Q. Zhao, S. Chen, B. Ren, S. Liu, Y. Zhang, X. Luo, W. Feng and Y. Sun, *Opt. Mater.*, **135**, 113266 (2023); https://doi.org/10.1016/j.optmat.2022.113266
15. M. Tiwari and G.C. Joshi, *J. Sol-Gel Sci. Technol*, (2024); https://doi.org/10.1007/s10971-024-06315-x
16. L.X. Lovisa, D.F. Dos Santos, A.A.G. Santiago, M.D. Teodoro, M.R.D. Bomio and F.V. Motta, *RSC Adv.*, **13**, 25738 (2023); https://doi.org/10.1039/D3RA05136F
17. F.A. Jan, M. Ahmad, U. Shah, M. Saleem, R. Ullah and N. Ullah, *J. Chem. Soc. Pak.*, **43**, 726 (2021).
18. V. Ramar and K. Balasubramanian, *ACS Appl. Nano Mater.*, **4**, 5512 (2021); https://doi.org/10.1021/acsanm.1c00863
19. B. Chai, J. Li, Q. Xu and K. Dai, *Mater. Lett.*, **120**, 177 (2014); https://doi.org/10.1016/j.matlet.2014.01.094
20. M. Zhou, J. Yan and P. Cui, *Mater. Lett.*, **89**, 258 (2012); https://doi.org/10.1016/j.matlet.2012.08.081
21. T. Govindaraj, C. Mahendran, V.S. Manikandan, J. Archana, M. Shkir and J. Chandrasekaran, *J. Alloys Compd.*, **868**, 159091 (2021); https://doi.org/10.1016/j.jallcom.2021.159091
22. L. Gan, L. Xu, S. Shang, X. Zhou and L. Meng, *Ceram. Int.*, **42**, 15235 (2016); https://doi.org/10.1016/j.ceramint.2016.06.160
23. A.A. Ismail, M. Faisal and A. Al-Haddad, *J. Environ. Sci.*, **66**, 328 (2018); https://doi.org/10.1016/j.jes.2017.05.001
24. X. Hu, P. Xu, H. Gong and G. Yin, *Materials*, **11**, 147 (2018); https://doi.org/10.3390/ma11010147
25. M.B. Tahir, S. Farman, M. Rafique, M. Shakil, M.I. Khan, I. Mubeen, M. Ijaz, M. Ashraf and K.N. Riaz, *Int. J. Environ. Anal. Chem.*, **101**, 1448 (2021); https://doi.org/10.1080/03067319.2019.1685093
26. M. Stan, D. Toloman, A. Popa, M. Dan, R.C. Suciu, S. Macavei, S.C. Tripon, K. Chaiseeda and O. Pana, *Synth. Met.*, **288**, 117117 (2022); https://doi.org/10.1016/j.synthmet.2022.117117
27. U. Younas, A. Ahmad, A. Islam, F. Ali, M. Pervaiz, A. Saleem, M. Waseem, A.M. Aljuwayid, M.A. Habila and S.R. Naqvi, *Fuel*, **349**, 128668 (2023); https://doi.org/10.1016/j.fuel.2023.128668
28. S. Ghattavi and A. Nezamzadeh-Ejhieh, *J. Mol. Liq.*, **322**, 114563 (2021); https://doi.org/10.1016/j.molliq.2020.114563
29. J. Tang, R. Meng, Y. Xue, S. Zhang and Q. Li, *Inorg. Chem. Commun.*, **132**, 108792 (2021); https://doi.org/10.1016/j.inoche.2021.108792
30. M. Liaqat, R.M. Munir, I. Maryam, T. Iqbal, S. Afsheen, A.G. Nabi, R.R.M. Khan, A. El-Marghany, I. Warad and A. Basit, *Mater. Chem. Phys.*, **320**, 129465 (2024); https://doi.org/10.1016/j.matchemphys.2024.129465

31. S. Sahoo, A. Rebekah and K.S. Lee, *APL Mater.*, **12**, 041122 (2024); https://doi.org/10.1063/5.0202943
32. G.M. Kumar, D.J. Lee, H.C. Jeon, P. Ilanchezhiyan, K.D. Young and K.T. Won, *Ceram. Int.*, **48**, 4332 (2022); https://doi.org/10.1016/j.ceramint.2021.10.228
33. S. Hemasankari, S. Priyadharshini, V. Sathiyanarayanamoorthi, N. Al Sdran, D. Thangaraju and M. Shkir, *Physica B*, **660**, 414870 (2023); https://doi.org/10.1016/j.physb.2023.414870
34. U. Shah, F.A. Jan, R. Ullah, Wajidullah, Salman and N. Ullah, *ECS J. Solid State Sci. Technol.*, **11**, 033011 (2022); https://doi.org/10.1149/2162-8777/ac5c7e
35. H.A. Mahmoud, T.T. Ali, S.A. Nasr, E.A.A. Mahmoud, L.A.E. Nassr and I.M.A. Mohamed, *J. Korean Ceram. Soc.*, **62**, 460 (2025); https://doi.org/10.1007/s43207-024-00472-z
36. M.T. Elabbasy, M.A. El-Morsy, N.S. Awwad, H.A. Ibrahium and A.A. Menazea, *Sci. Rep.*, **14**, 9877 (2024); https://doi.org/10.1038/s41598-024-57226-4
37. K. Narasimharao and T.T. Ali, *J. Mater. Res. Technol.*, **9**, 1819 (2020); https://doi.org/10.1016/j.jmrt.2019.12.014
38. S. Velmurugan, K.J. Jothi, I. Pakrudheen, S. Nagarani, S. Mubarak, S. Devanesan and M.S. AlSalhi, *Ceram. Int.*, **51**, 6627 (2025); https://doi.org/10.1016/j.ceramint.2024.12.107
39. H. Liu, J. Huang, J. Chen, J. Zhong, J. Li and R. Duan, *Solid State Sci.*, **95**, 105923 (2019); https://doi.org/10.1016/j.solidstatesciences.2019.06.012
40. H.I. Rizvi, R.M. Munir, T. Iqbal, A. Younas, S. Afsheen, M.T. Qureshi, L. Aamir, M.A. Elaimi, K. Sultana, K.N. Riaz and M. Yousaf, *J. Alloys Compd.*, **993**, 174549 (2024); https://doi.org/10.1016/j.jallcom.2024.174549
41. G. Jeevitha, R. Abhinayaa, D. Mangalaraj and N. Ponpandian, *J. Phys. Chem. Solids*, **116**, 137 (2018); https://doi.org/10.1016/j.jpcs.2018.01.021
42. S. Siddique, Zain-ul-Abdin, M. Waseem, T. Naseem, A. Bibi, M. Hafeez, S.U. Din, S. Haq and S. Qureshi, *J. Inorg. Organomet. Polym. Mater.*, **31**, 1359 (2021); https://doi.org/10.1007/s10904-020-01760-x
43. A.B. Habtemariam and Y. Alemu, *Biointerface Res. Appl. Chem.*, **12**, 529 (2021); https://doi.org/10.33263/BRIAC121.529536
44. V. Uthiravel, K. Narayanamurthi, V. Raja, S. Anandhabasker and K. Kuppusamy, *Inorg. Chem. Commun.*, **170**, 113327 (2024); https://doi.org/10.1016/j.inoche.2024.113327